Chemically and Electrochemically Stable Nb_2O_5 Protection Layers for Hydrogen Evolution by p-InP Photocathodes in Acidic Electrolytes

Alexandre Z. Ye[1], Dominic Covelli[1], Ariel A. Struzyk[1], Paul J. L. Bean[1], Xinyi Elaine Shen[1], Nathan S. Lewis[1,2,]*

1. Division of Chemistry and Chemical Engineering, California Institute of Technology, Pasadena, CA 91125, United States

2. Beckman Institute, California Institute of Technology, Pasadena, CA 91125, United States

*Corresponding author. nslewis@caltech.edu

ABSTRACT

Coatings of HfO_2, Ta_2O_5, TiO_2, and Nb_2O_5 were evaluated as protection layers for p-InP photocathodes in aqueous acidic electrolytes. Each candidate protection layer was characterized based on interfacial conduction of photogenerated electrons, the thermodynamic and kinetic stability of the overlayer over the relevant potential and pH range for cathodic fuel-forming half-reactions, and inhibition of the primary anodic and/or chemical dissolution processes that limit electrode stability. The conduction of photogenerated electrons and inhibition of anodic oxidation was evaluated using $V^{3+/2+}$ in 5.0 M HCl(aq) as a one-electron redox couple with a potential close to that of hydrogen evolution in acidic media. Failure modes due to cathodic plating of metal, as well as anodic dissolution and chemical dissolution processes, were evaluated for photocathodes made from etched p-InP, platinized p-InP, and p-InP photoelectrodes that had been coated with the various oxide films and then platinized for use in photoelectrochemical hydrogen evolution in acidic aqueous electrolytes. Nb_2O_5 best met all of the criteria, contrasting with TiO_2 which is thermodynamically and kinetically unstable in acid over the potential range relevant for the hydrogen evolution and/or CO_2 reduction electrochemical half-reactions. These protocols should be useful on other materials and semiconductors to determine the effectiveness of protection layers for photocathodes.

TOC GRAPHICS

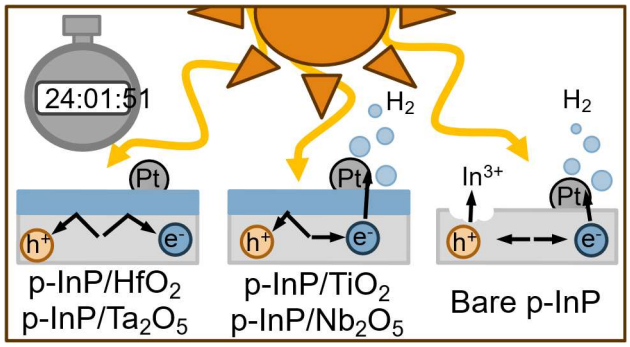

Introduction

Semiconductor photoelectrodes are generally unstable in the electrolytes required for safe, efficient oxidation of H_2O to $O_2(g)$, in conjunction with the reduction of H_2O and/or CO_2 to produce solar fuels.[1–3] Many semiconducting photoanodes have been stabilized by protection layers, with an emphasis on use of TiO_2 deposited by atomic layer deposition (ALD) methods.[4–6] TiO_2 is stable thermodynamically under alkaline conditions at positive potentials,[7] thus enabling photoanodes to efficiently sustain the oxygen-evolution reaction. Moreover, 50-60 nm thick TiO_2 films formed by atomic layer deposition provide facile hole conduction to a variety of water oxidation catalysts while protecting the underlying semiconductor from corrosion in 1.0 M KOH(aq).[5,8–10] Specifically, Si microwire array photoanodes have yielded high photoelectrode energy-conversion efficiencies for $O_2(g)$ production for thousands of hours of continuous operation under simulated sunlight.[11]

In contrast to photoanodes, protection layers for fuel-forming photocathodes do not require a defect band to effect rapid hole conduction but instead should allow conduction of photogenerated electrons at or near the potential of the reversible hydrogen electrode (RHE). Moreover, instead of anodic passivation or corrosion by dissolution, the failure modes of photocathodes include cathodic plating of metal, reductive dissolution of the atomic constituents of the semiconducting photoelectrode, and chemical dissolution and dark anodic corrosion at open circuit.[12–15] Additionally, photocathode protection layers need to be stable chemically and electrochemically under more negative potentials than are experienced by photoanodes performing water oxidation.

III-V semiconductor alloys, such as alloys of GaAs, InP, and/or GaP, can have band gaps ($\mathbf{E}_g$) of ~1.7 eV, and thus would provide photocathodes that could be paired with oxygen-evolving Si photoanodes to produce a tandem photoelectrochemical cell with nearly optimal energy-

conversion efficiency for solar fuel production.[16,17] At very negative potentials, p-type GaInP and p-InP undergo photocorrosion by plating of metallic In.[12,13,18–20] However, p-InP (and p-GaInP) can be kinetically stabilized for H_2 production by addition of a Pt catalyst that prevents the minority-carrier quasi-Fermi level from becoming sufficiently negative in potential to reduce InP to In^0.[12,21] p-InP is thus a Type II semiconductor as classified by Gerischer,[15,22] and consequently under continuous simulated solar illumination, p-InP/Pt photoelectrodes provide stable, 12% efficient photoelectrodes for H_2 production in 1.0 M HCl(aq).[21] Nanopillars of p-InP protected by 5 nm TiO_2 and coated with Ru as a catalyst for the hydrogen-evolution reaction (HER) have exhibited stable photocurrent for H_2 evolution for >4 h in 1 M $HClO_4$(aq) at 0.23 V vs RHE.[23] p-$GaInP_2$ protected by a catalytically active barrier layer of MoS_2 showed photocurrent stability for >60 h in 3 M H_2SO_4(aq) at -0.025 V vs RHE, compared to bare p-$GaInP_2$, which lasted <5 h,[20] as expected for Type II kinetic stabilization of p-InP and p-$GaInP_2$ photocathodes under illumination.[15,22] p-GaP photocathodes coated with reactively sputtered Nb_2O_5 and a Pt HER catalyst yielded stable photocurrents for <16 h under illumination at 0.63 V vs RHE in 1 M $HClO_4$(aq).[24] Also, n^+p-Si photocathodes that were spin-coated with Nb_2O_5 followed by deposition of a NiPt catalyst produced stable photocurrents for 100 h at 0 V vs RHE in 0.5 M H_2SO_4.[25] Notably, due to cathodic protection, p-GaP, p-Si, and n^+p-Si photocathodes are kinetically stabilized by Pt and consequently yield stable photocurrents while effecting the HER in acid,[13,26,27] confounding conclusions regarding potential benefits of a protection layer for such systems. The primary failure mode of kinetically stabilized p-InP/Pt and related III-V/catalyst photocathodes is irreversible reduction of the interfacial oxide in conjunction with anodic dissolution and/or chemical dissolution of the photoelectrode material at or near open-circuit in the dark, as opposed

to degradation while passing cathodic current under illumination near the maximum power point of the cell.[12,13,21]

In this work, a series of metal oxides (TiO_2, Nb_2O_5, HfO_2, and Ta_2O_5) with different band gaps and conduction band-edge positions was systematically evaluated as protection layers for p-InP photocathodes. Desirable properties include facile conduction of photogenerated electrons for reduction reactions at potentials near RHE, chemical and electrochemical stability under acidic conditions, and the ability to suppress the relevant primary failure modes of chemical dissolution and anodic dissolution near the open-circuit potential in the dark. The approach moreover illustrates a protocol to determine the effectiveness of a protection layer for photocathodes that are kinetically stabilized from decomposition under continuous illumination and consequently should exhibit a stable photocurrent for extended time periods when operated solely under those specific test conditions without any protection layer present.

Materials and Methods

Materials

p-type InP wafers (ATX Inc.) were (100)-oriented, single-side polished, and Zn-doped (N_d = 1-8×10^{17} cm^{-3}). The following reagents were used as received: bromine (Br_2, ACS reagent grade, Sigma Aldrich), methanol (CH_3OH, 99.8%, ACS, VWR Analytical), ammonium hydroxide (NH_4OH, 28-30%, ACS, Sigma Aldrich), conductive silver paint (PELCO, Ted Pella, Inc), epoxy (Hysol-9460), vanadium (V) oxide (V_2O_5, >99.6% trace metal basis, Sigma Aldrich), zinc (Zn, granular, Acros Organics), mercury (Hg, 99.9998%, Alfa Aesar), potassium tetrachloroplatinate (II) (K_2PtCl_4, 99.9% - Pt, STREM), potassium chloride (KCl, ACS, Macron), hydrochloric acid (HCl, ACS, Sigma Aldrich), nitric acid (HNO_3, ACS, Sigma Aldrich), sulfuric acid (H_2SO_4, 95.0-98.0%, ACS, JT Baker), hydrogen (H_2, UHP, Airgas), oxygen (O_2, UHP, Airgas), argon (Ar, UHP,

Airgas) and nitrogen (N_2, UHP, Airgas). The niobium precursor ((t-Butylimido)tris(diethylamino)niobium(V), 98%+, STREM), titanium precursor (Tetrakis(dimethylamido)titanium(IV), 99.999%, Sigma Aldrich), hafnium precursor (Tetrakis(dimethylamino)hafnium(IV), 98%+, STREM), and tantalum precursor (Pentakis(dimethylamino)tantalum(V), 98%+, STREM), were loaded into new ALD cylinders in a N_2-purged glovebox that contained <10 ppm O_2. Ultrahigh purity water (18.2 MΩ cm, Thermo Scientific Nanopure system) was used as the oxidant during ALD and for making electrochemical solutions. The H_2SO_4 was diluted with water to 1.0 M for electrochemical experiments.

InP Etching and Ohmic Contacts

Ohmic back contacts were made to p-type InP wafers via a two-step sputtering and subsequent annealing process. First, 10 nm of Zn was sputtered onto the wafers, followed by 90 nm of Au. Sputter deposition was performed in a custom-built RF sputtering system with a base pressure of 5×10^{-7} Torr. The sample was rotated during the deposition, and sputtering was performed under 2 mTorr Ar at 60-70W, at a rate of 0.8 Å s^{-1} as measured by a quartz microbalance, until the desired film thickness was obtained. The sample was then annealed under forming gas for 10 min at 400 °C.

Prior to electrochemical measurements and before the deposition of protection layers, the p-InP electrodes or wafers were etched in 0.04% (by volume) Br_2/CH_3OH for 30 s, followed by 1:1 (by volume) NH_4OH/H_2O for 30 s, and then rinsed with pure CH_3OH for 10 s. The etching and rinsing cycles were repeated twice, and the p-InP was dried under a stream of N_2.

Deposition of Metal Oxides

Niobium oxide was deposited via a Cambridge Nanotech Savanah S200 Atomic Layer Deposition (ALD) System. The TBTDEN was heated to 120 °C, the H_2O was kept at room temperature, and the reactor was heated to 250 °C. The deposition consisted of 0.15 s pulses of TBTDEN, a 15 s purge with 20 sccm N_2, 0.015 s of H_2O, and a 60 s purge. Approximately 1200 cycles were used to deposit ~50 nm of Nb_2O_5. The thickness of the Nb_2O_5 film was determined across a wavelength range of 380-890 nm at 65, 70, and 75° angles, using a J.A. Woolam Co ellipsometer with the CompleteEASE software.

The other metal oxides TiO_2, HfO_2, and Ta_2O_5 were deposited in an analogous manner using slightly different parameters (Table 1).

Table 1. ALD parameters for metal oxide depositions

Metal Oxide	TiO_2	HfO_2	Ta_2O_5	Nb_2O_5
Precursor Temperature	90 °C	90 °C	120 °C	120 °C
Reactor Temperature	150 °C	150 °C	150 °C	250 °C
Precursor Pulse Duration	0.15 s	0.15 s	0.15 s	0.15 s
Purge Duration Following Precursor Pulse	15 s	15 s	15 s	15 s
Water Pulse Duration	0.015 s	0.015 s	0.015 s	0.015 s
Purge Duration Following Water Pulse	15 s	15 s	15 s	60 s
Approximate Deposition Rate (Number of cycles used for 50 nm films)	0.5 Å/cycle (1000 cycles)	1.1 Å/cycle (460 cycles)	0.45 Å/cycle (1100 cycles)	0.4 Å/cycle (1200 cycles)

Electrode Fabrication

For electrochemical measurements, the back contact to the InP sample was attached to a coiled, tin-plated Cu wire (McMaster-Carr) using Ag paint. The electrode was then allowed to dry for at least 1 h and the Cu wire was then threaded through a piece of glass tubing (Corning Incorporated, Pyrex tubing, 7740 glass). The sample was encapsulated in, and sealed to, the glass tube using Hysol-9460 epoxy, which was allowed to dry overnight under ambient conditions. The exposed area of each electrode was then imaged using a high-resolution optical scanner (Epson Perfection V370 with a resolution of 1200 dpi), and the geometric areas of the electrodes (typically 0.07-0.10 cm^2) were analyzed using ImageJ software.

For Ni electrodes, glass slides were cleaned with isopropyl alcohol and dried under a stream of $N_2(g)$. 50 nm Ni was then evaporated onto the glass slides with a Denton Explorer 14 electron-beam metal evaporator with a base pressure of $<10^{-6}$ torr using an accelerating voltage of 10 kV and 70 mA deposition current. The Ni-coated glass slides were then cut and used to make electrodes in the same manner as the InP samples.

Electrochemical Measurements

Before use, electrochemical cells were cleaned using a 3:1 volume ratio of $HCl:HNO_3$. Electrochemical measurements were performed without IR compensation using a SP-200 potentiostat (BioLogic Science Instruments). The light source was an ENH-type W-halogen lamp, and the intensity was calibrated to be equivalent to 100 mW cm^{-2} of Air Mass 1.5 illumination using a calibrated silicon photodiode (FDS100-Cal, Thor Labs) that was placed at the same position as the working electrode.

A three-electrode set-up with a graphite rod as the counter electrode, and an SCE reference electrode (CHI) was used for cells that contained $V^{3+/2+}$ in 5.0 M HCl(aq). The cell was purged

with N_2(g) before and during collection of electrochemical data. Cathodic *J-E* behavior was measured with a scan rate of 50 mV s^{-1} starting from -0.46 V vs SCE (~ $E(V^{3+/2+})$) to a potential of < -0.6 V vs SCE, then to E_{oc}, and finally to -0.46 V vs SCE. The anodic *J-E* behavior was measured at a scan rate of 50 mV s^{-1} from -0.46 V vs SCE (~ $E(V^{3+/2+})$) to 0.6 V vs SCE and ending at -0.46 V vs SCE.

For stability measurements in 1.0M H_2SO_4(aq), a Teflon compression cell was used to avoid the leaching of ions through the epoxy of glass body electrodes. A peristaltic pump was used to dislodge gas bubbles from the surface of the electrode. A Pt wire RHE was used as the reference electrode, and the counter electrode was a separate Pt wire that was separated from the main compartment using a ground glass frit. The cell was purged with H_2 before and during the experiment, and the cell was stirred. 200 µL of the electrolyte was removed from the hydrogen outlet for ICP-MS analysis periodically without replacement. The overall cell volume was 30 mL. *J-E* behavior of the electrodes was determined periodically every 2 h by first interrupting the chronoamperometry with a short 15 s open circuit condition to measure E_{oc}. Then, the *J-E* behavior was measured by starting from $E_{start} = E_{oc} - 30$ mV to a vertex potential of < 0 V vs RHE and ending at $E_{end} = E_{oc} - 80$ mV. These potentials were chosen to minimize the anodic current through the electrode. Two *J-E* scans were collected during each current interruption. Voltammetry was collected at a scan rate of 50 mV s^{-1}.

Electrodeposition of Pt

Pt nano-islands were electrodeposited in a two-electrode configuration using a Pt(II) solution (5 mM K_2PtCl_4 in 0.5 M KCl) at a current density of -0.2 mA cm^{-2} until 20 mC cm^{-2} had passed. The

electrodeposition was performed under ~1 Sun of simulated solar illumination. A Pt wire was used as the counter electrode.

Preparation of $V^{3+/2+}$ Solutions

A $V^{3+/2+}$ solution that contained a total vanadium concentration of 350 mM was prepared by stirring V_2O_5 in water and slowly adding, over several hours under a N_2 purge, concentrated HCl dropwise to the solution until a 5.0 M HCl(aq) solution was obtained. The dissolved V^{5+} was then reduced to V^{2+} by adding a Zn (Hg) amalgam until the V was fully reduced. The color of the solution turned from orange to green and finally to blue violet. The solution potential was then brought from -0.51 V vs SCE to -0.46 V vs SCE by bubbling O_2 into the cell.

Mott-Schottky Measurements

Mott-Schottky measurements were performed using an SP-200 potentiostat (BioLogic Science Instruments) in contact with 350 mM $V^{3+/2+}$-5.0 M HCl(aq) or 1.0 M H_2SO_4(aq) under a stream of flowing N_2(g) or H_2(g), respectively. The impedance data were collected in the dark in the reverse bias region with a sinusoidal wave amplitude of 10 mV over a frequency range of 100 kHz to 10 Hz. The impedance measurements were fit to a model circuit consisting of a resistor in series with a component consisting of a resistor and capacitor in parallel. The potential dependence of the differential capacitance was analyzed using the Mott-Schottky equation:

$$C_d^{-2} = \frac{2}{qA^2\epsilon_0\epsilon_r N_d}\left(V_{app} + V_{bi} - \frac{k_B T}{q}\right)$$

Here, C_d is the differential capacitance, q is the unsigned charge of an electron, A is the area of the electrode, $\epsilon_0$is the vacuum permittivity, ϵ_r is the relative permittivity of the semiconductor, N_d is the dopant concentration of the semiconductor, V_{app} is the applied electrode potential, V_{bi} is the

built-in voltage in the semiconductor, k_b is the Boltzmann constant, and T is the temperature of the electrode while the impedance data were collected. A relative permittivity of $\epsilon_r = 8.8$ was used for InP. The slopes of the Mott-Schottky relationship were used to calculate the dopant density, N_d. The dopant density extracted from the slope of C_d^{-2} vs V_{app} was then compared to the dopant density of the sample provided by the manufacturer, to verify the accuracy of the fit to the Mott-Schottky data.

SEM Data

Scanning-electron micrographs (SEMs) were obtained using a calibrated Nova NanoSEM 450 (FEI) at an accelerating voltage of 5 kV with a working distance of 5.0 mm and an in-lens secondary electron detector.

X-ray Photoelectron Spectroscopy Measurements

X-ray photoelectron spectroscopy (XPS) was performed using a Kratos Axis Ultra system with a base pressure of 3×10^{-9} Torr in the analysis chamber. A 150 W monochromatic Al Kα source was used to irradiate the sample with X-rays (1486.6 eV). For maximum depth sensitivity, the hemispherical analyzer was oriented for detection along the sample surface normal. The data were analyzed using CasaXPS software. A Shirley background was used for all spectra, and all peaks were referenced to adventitious C at a binding energy of 284.8 eV. The Pt^0 peak of the Pt 4f spectra was fit using an asymmetric peak shape (LA(1.2, 85, 70) in CasaXPS). All other peaks were fit using a 50% Gaussian/50% Lorentzian Voigt-function (LA(50) in CasaXPS).

UV-Visible Spectroscopy

Ultraviolet-visible spectroscopy between 190-1100 nm was performed on an Agilent 8453 UV-vis Spectrometer. 50 nm of either Nb_2O_5 or TiO_2 was deposited on fluorine-doped tin oxide (FTO, Tec 8) samples that were then cut into 1 cm x 5 cm pieces. The pieces were used as part of a single compartment 3-electrode cell with the coated FTO acting as the working electrode, along with a Pt wire counter electrode and a 3.0 M KCl Ag/AgCl reference electrode. The electrolyte was 1.0 M H_2SO_4(aq). The UV-Vis was blanked after holding the working electrode for 15 min at 0.8 V vs Ag/AgCl. The potential was swept from 0.8 V vs Ag/AgCl to -0.8 V vs Ag/AgCl at 5 mV s^{-1}, and UV-Vis spectra were taken every 2 s.

ICP-MS Measurements

ICP-MS was performed using an Agilent 8800 Triple Quadrupole ICP-MS system. Calibration samples were prepared by diluting standard solutions for ICP with water having a resistivity of 18.2 MΩ cm. All samples were diluted using 5% (~0.8 M) nitric acid to pH < 2. The concentration of In dissolved in the electrolyte sample was then used to calculate the equivalent depth of InP removed from the InP electrode normalized by the geometric electrode surface area.

Results

Conduction of Photogenerated Electrons in Contact with $V^{3+/2}$-5.0 M HCl(aq)

Figure 1a shows the current density vs potential (*J-E*) behavior in 350 mM $V^{3+/2+}$-5.0 M HCl(aq) of illuminated p-InP photocathodes coated with ~50 nm of ALD-deposited TiO_2, Nb_2O_5, HfO_2, or Ta_2O_5. The metal oxides were deposited using 1000 cycles of tetrakis(dimethylamido)titanium(IV) (TDMAT) at 150 °C for TiO_2, 1200 cycles of (t-Butylimido)tris(diethylamino)niobium(V) (TBTDEN) at 250 °C for Nb_2O_5, 460 cycles of tetrakis(dimethylamino)hafnium(IV) (TDMAH) at 150 °C for HfO_2, and 1100 cycles of pentakis(dimethylamino)tantalum(V) (PDMAT) at 150 °C

for Ta_2O_5. The complete deposition conditions and electrode fabrication procedures are listed in the methods. 50 nm was chosen to minimize pinholes in the barrier layers[5,28] and to maximize conductivity of the barrier layers. However, the film thickness could be optimized further in specific cases such as for anti-reflective coatings or to reduce the resistance of the films to obtain enhanced performance. The Nernstian potential of the cell, $E(V^{3+/2+})$, was -0.46 V vs SCE. Etched p-InP as well as p-InP coated with Nb_2O_5 or TiO_2 exhibited light-limited current densities of -10 mA cm^{-2} at -0.7 V vs SCE. In contrast, p-InP coated with HfO_2 or Ta_2O_5 produced $|J|$ = <0.5 mA cm^{-2} at potentials <-0.8 V vs SCE (Figure 1a). p-InP/TiO_2 and p-InP/Nb_2O_5 electrodes produced photovoltages that were ~560 mV and ~400 mV, respectively, less than the photovoltages produced by etched p-InP electrodes. Mott-Schottky analyses derived from the differential capacitance vs potential behavior of p-InP, p-InP/TiO_2, and p-InP/Nb_2O_5 contacts produced flat-band potentials, E_{fb}, of 0.64 V, 0.58 V, and 0.50 V vs SCE, respectively (Figure S1a and S2). The dopant densities of the Mott-Schottky fits were in accord with the dopant density specified by the manufacturer (Figure S1). The InP/TiO_2 electrodes showed visible thinning of the TiO_2 coating after an hour of electrochemical testing in the $V^{3+/2+}$-5.0 M HCl(aq) solution. The HfO_2 and Ta_2O_5 were too resistive to obtain reliable Mott-Schottky behavior, and the TiO_2 data may be confounded by the rapid dissolution of the film at or near the pH values of interest.

X-ray photoelectron spectroscopy (XPS) confirmed the composition and oxidation state of the ALD-deposited metal oxides. The p-InP/Ta_2O_5 sample had a Ta $4f_{7/2}$ binding energy of 25.9 eV attributable to Ta_2O_5, and the p-InP/HfO_2 sample had a Hf $4f_{7/2}$ binding energy of 16.7 eV attributable to HfO_2.[29] The p-InP/Nb_2O_5 sample had a Nb $3d_{5/2}$ binding energy of 207.3 eV indicative of Nb_2O_5, and the p-InP/TiO_2 sample had a Ti $2p_{3/2}$ binding energy of 458.5 eV

indicative of TiO_2 (Figure S3).[29] These ALD-deposited metal oxide films were amorphous, as indicated by x-ray diffraction (XRD) data.

In 5.0 M HCl(aq), $V^{3+/2+}$ is a one-electron redox couple that allows oxidation and reduction at the surface of the photocathodes without concurrent corrosion of p-InP. $V^{3+/2+}$ yields high efficiency junctions with p-InP photoelectrodes, and both forms of the $V^{3+/2+}$ redox species are very soluble in aqueous acid, minimizing mass transport issues that could limit the photocurrent density.[30] Both forms of the redox couple have optical absorptions dominated by optically forbidden d-d transitions, and the $V^{3+/2+}$ system thus also minimizes any reduction in photocurrent due to absorption by the redox species in the electrolyte, while being within 0.2 V of RHE in acidic media.[30] Other redox couples such as methyl viologen ($E^0(MV^{2+/+})$ = -0.446 V vs the standard hydrogen electrode, SHE)[31] and $Eu^{3+/2+}$ ($E^0(Eu^{3+/2+})$ = -0.34 V vs SHE)[32] have redox potentials further from $E(H^+/H_2)$ than $V^{3+/2+}$ ($E(V^{3+/2+})$ = -0.22 V vs SHE). MV^+ moreover absorbs strongly throughout the visible region of the spectrum even at modest (>1 mM concentrations in the electrolyte). Furthermore, $Eu^{3+/2+}$ is only quasi-reversible in many aqueous solutions.[32]

Figure S4 presents a band diagram scheme depicting the relative positions of the conduction bands and redox potentials. The potential of the conduction-band edge, E_{cb}, of HfO_2, and $E_{cb}(Ta_2O_5)$, are much more negative than E_{cb}(InP), creating a substantial energetic barrier that inhibits the transfer of photogenerated electrons across the p-InP/metal oxide interface (Figure S4).[33–35] In contrast, $E_{cb}(TiO_2)$ and $E_{cb}(Nb_2O_5)$ are close to E_{cb}(InP) as evidenced by the similar flat-band potentials measured by Mott-Schottky analysis (Figure S1). The relative band-edge positions for the various oxides determined by ultraviolet photoelectron spectroscopy, UPS, are consistent with the observed behavior, although ultra-high vacuum methods do not fully account for the pH dependence of the flat-band potentials of metal oxides in aqueous solutions due to

protonation reactions of the surface or any differences in protonation state between the oxide/liquid and oxide/p-InP interfaces.[36,37] Table S3 lists literature values of E_{cb} for HfO_2, Ta_2O_5, TiO_2, Nb_2O_5, and InP. The band gap of Nb_2O_5 depends on the crystal phase, but $\mathbf{E}_g$ for Nb_2O_5 is typically ~3.5 eV,[38,39] as compared to $\mathbf{E}_g$ ~3.0 eV for rutile TiO_2.[40,41] The potentials of the valence-band edge (E_{vb}) of metal oxides are generally dominated by the energy of the O 2p level, so E_{vb} is relatively constant between different metal oxides.[40,42–44] Consequently, the difference in $\mathbf{E}_g$ between Nb_2O_5 and TiO_2 is expected to yield $E_{cb}(Nb_2O_5) < E_{cb}(TiO_2)$. Consistently, E_{cb}(InP) is ~-0.4 V vs RHE, $E_{cb}(TiO_2)$ is ~0.1-0.2 V vs RHE, and $E_{cb}(Nb_2O_5)$ is ~ -0.3 V vs RHE (Figure S4).[44,45]

The difference in electrochemical response between TiO_2-, Nb_2O_5-, HfO_2-, and Ta_2O_5-coated p-InP photocathodes (Figure 1a) is consistent with expectations that lowered energetic barriers at the protection layer/liquid interface improve the conduction of photogenerated electrons into the $V^{3+/2+}$-5.0 M HCl(aq) solution. The difference in the photovoltages produced by the p-InP, p-InP/TiO_2 and p-InP/Nb_2O_5 electrodes is also consistent with the measured differences in E_{fb} in conjunction with the different energetic barriers between the metal oxide protection layers and the $V^{3+/2+}$(aq) -5.0 M HCl(aq) electrolyte. The more negative value of $E_{cb}(Nb_2O_5)$ relative to $E_{cb}(TiO_2)$ is expected to produce a higher energetic barrier for reduction of V^{3+} by TiO_2-coated electrodes than by Nb_2O_5-coated electrodes (Figure S4, S5a, and S6), in accord with the *J-E* behavior observed in Figure 1a. Relative to an etched Ni electrode, Ni/TiO_2 and Ni/Nb_2O_5 electrodes exhibited shifts of ~ -400 mV and ~ -250 mV, respectively, in the *J-E* behavior for reduction of $V^{3+/2+}$(aq) (Figure S5a), in accord with expectations for $E_{cb}(Nb_2O_5) < E(V^{3+/2+}) < E_{cb}(TiO_2)$. The photocurrent density observed on all of the p-InP electrodes is less than the maximum theoretical photocurrent density (~28 mA cm^{-2})[21] under 100 mW cm^{-2} of simulated solar illumination due to a long path length in the blue-violet $V^{3+/2+}$ solution and optical reflection losses.

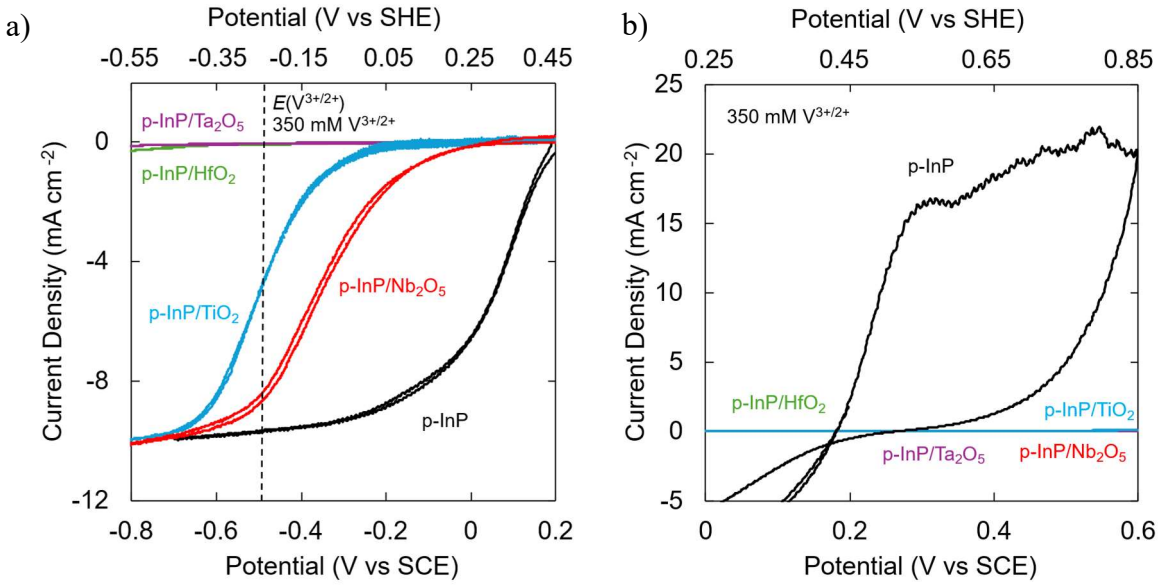

Figure 1. *J-E* behavior of (a) the cathodic region and (b) the anodic region of illuminated p-InP electrodes coated with different barrier layers in a 350 mM solution of $V^{3+/2+}$ in 5.0 M HCl(aq). The solution potential was -0.46 V vs SCE.

Effect of Pinholes on the Performance and Stability of p-InP/oxide Photocathodes in Contact with $V^{3+/2+}$-HCl(aq)

Figure 1b shows the *J-E* behavior of p-InP/TiO_2, p-InP/Nb_2O_5, p-InP/HfO_2, and p-InP/Ta_2O_5 electrodes at potentials positive of the open-circuit potential, E_{oc}, in contact with 350 mM $V^{3+/2+}$-5.0 M HCl(aq). Etched p-InP electrodes passed >20 mA cm^{-2} of anodic current density at $E > 0.3$ V vs SCE, whereas under the same conditions the samples coated with metal oxide protection layers passed <1 mA cm^{-2} of anodic current density. Stable photocurrents for kinetically stabilized photocathodes performing the HER could be obtained with a fully insulating oxide overlayer by flow of charge through pinholes or uncoated areas of the photoelectrode of interest, without substantially affecting the primary failure mode of such systems, so identifying the role of pinholes

on the photoelectrochemical behavior is important in understanding the conductivity of these barrier layers. The small limiting anodic current density of the coated p-InP electrodes indicates that the metal oxide coatings suppress transfer of holes from the semiconductor to the electrolyte, reducing the rate of anodic dissolution of InP. The data demonstrate that the interfacial charge transfer occurs predominantly through the Nb_2O_5 films.

The remaining anodic current density is consistent with exposure to the electrolyte of ~0.1% of the surface area of the coated samples, based on studies of GaAs photoanodes that were coated with oxides deposited in air by ALD.[28,46] The change in photovoltage between the etched p-InP electrodes and the coated p-InP electrodes (Figure 1a) indicates that the voltametric behavior is determined by the p-InP/oxide/liquid interfacial structure as opposed to being determined by pinhole-exposed areas that produce direct contact between the p-InP and the $V^{3+/2+}$ electrolyte. Furthermore, the mutually similar light-limited current densities observed for TiO_2-coated, Nb_2O_5-coated, and etched p-InP electrodes indicate that electrons flow through the coated areas of the TiO_2- and Nb_2O_5-coated samples as opposed to flowing solely through pinholes in the protection layers.

Stability of p-InP/Nb_2O_5 Photocathodes for Hydrogen Evolution

Figure 2a shows the *J-t* behavior of p-InP, p-InP/Pt, p-InP/Nb_2O_5, and p-InP/Nb_2O_5/Pt electrodes held at 0 V vs RHE in 1.0 M H_2SO_4(aq) under 100 mW cm^{-2} of simulated solar illumination. Within 30 min, the cathodic current density of etched p-InP electrodes decreased from ~6 mA cm^{-2} to <0.1 mA cm^{-2}. Under these conditions a visible film of off-white/grey In/InO_x, indicative of photocorrosion, formed rapidly on the etched p-InP electrode.[12]

p-InP/Nb_2O_5 electrodes initially exhibited cathodic current densities of $|J| < 0.1$ mA cm^{-2}, with a steady increase in cathodic current density after 6 h to $|J| > 1$ mA cm^{-2}. The current density

fluctuated over the remaining 18 h of the experiment. The gradual increase in current density after the initial 6 h of the p-InP/Nb_2O_5 electrode is consistent with reduction of the Nb_2O_5 layer into a more conductive phase, and/or cathodic plating of In^0 at exposed pinhole sites. In^0 is a relatively inactive catalyst for the HER but may catalyze the HER more effectively than Nb_2O_5. In contrast, p-InP/Pt and p-InP/Nb_2O_5/Pt electrodes produced J = -17 mA cm^{-2} for 24 h of continuous operation at 0 V vs RHE.

Properties of p-InP/TiO_2, p-InP/Ta_2O_5, and p-InP/HfO_2 Photocathodes for Hydrogen Evolution

InP/TiO_2 and InP/TiO_2/Pt electrodes held at 0 V vs RHE in 1.0 M H_2SO_4(aq) for 24 h under 100 mW cm^{-2} illumination resulted in dissolution of the TiO_2 film. Figures S7 and S8 show optical images and XPS data of TiO_2-coated electrodes before and after electrochemical testing, indicating that TiO_2 was no longer present after electrochemical testing.

HfO_2 and Ta_2O_5 did not facilitate interfacial electron flow at negative potentials even with a one-electron redox couple in solution (Figure 1), so these materials are unsatisfactory as photocathode protection layers despite their chemical stability at or near $E(H^+/H_2)$ in acidic electrolytes.[7] According to the Pourbaix diagrams, TiO_2 is thermodynamically stable at $E(H^+/H_2)$ under alkaline conditions but corrodes at $E(H^+/H_2)$ in acidic conditions.[7] The rapid dissolution of the TiO_2 film (Figure S7 and S8) under operating conditions for the HER underscores the ambiguity associated with phenomenological stability measurements, such as the number of consecutive hours of photocurrent stability, for photocathodes that are kinetically stabilized in the absence of any protection layer. Nb_2O_5 is thermodynamically stable over the entire pH and potential range of interest,[7,25,47] in contrast to TiO_2 and other metal oxides with $E_{cb} < E(H^+/H_2)$ in 1.0 M H_2SO_4(aq), such as $BaTiO_3$, $SrTiO_3$, and SnO_2.[7,43,48,49] Hence, of the metal oxides tested, on the basis of chemical stability Nb_2O_5 was the most suitable oxide for use as a protection layer for p-InP.

TiO_2 displays an optical absorption peak at 375 nm that is associated with Ti^{3+} defects.[50] When held at or near $E(H^+/H_2)$ in 1.0 M H_2SO_4(aq), the TiO_2 film formed a visible blue color (Figure S9a).[50] In contrast, spectroelectrochemical measurements showed that the Nb_2O_5 sample did not exhibit a distinctive absorption in this spectral range under potential control at 0 V vs RHE (Figure S9b). Consistently, in 1.0 M H_2SO_4(aq), electrochromism of Nb_2O_5 onsets at potentials <0 V vs RHE,[51] whereas electrochromism of TiO_2 onsets at ~0.2 V vs RHE.[50] Both oxides showed an increased background absorption throughout the potential sweep that resulted from scattering by evolved H_2 gas bubbles. Electrochromism of TiO_2 requires time to develop at steady state and thus affect the spectral absorption of the barrier layer.[50] Additionally, the spectrum of the light source used in these experiments, an ENH-type tungsten halogen lamp with a dichroic rear reflector,[52] is red-shifted compared to the Air Mass 1.5 solar spectrum.[53] Hence, unlike TiO_2, Nb_2O_5 films do not decrease the light-limited photocurrent density or result in trap states near the conduction-band edge while effecting the HER in aqueous electrolytes.

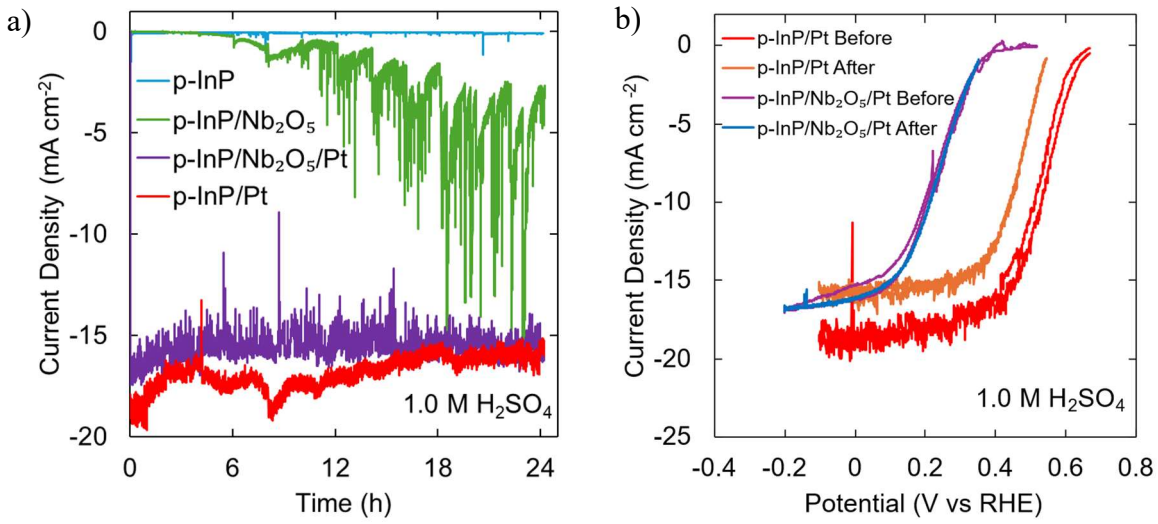

Figure 2. (a) *J-t* behavior of p-InP electrodes with Nb_2O_5 with or without Pt in 1.0 M H_2SO_4(aq) held at 0 V vs RHE under illumination. (b) *J-E* behavior of p-InP/Pt and p-InP/Nb_2O_5/Pt electrodes before and after the 24 h hold.

Electrochemical and Chemical Stability of p-InP/Nb_2O_5 Photocathodes for Hydrogen Evolution

Figures 2b show the *J-E* behavior of p-InP/Pt and p-InP/Nb_2O_5/Pt electrodes before and after, respectively, 24 h at 0 V vs RHE. Figure S10 shows the *J-E* behavior of p-InP and p-InP/Nb_2O_5 electrodes before and after, respectively, 24 h at 0 V vs RHE. After 24 h of continuous operation, the open-circuit potential, E_{oc}, of the p-InP/Pt electrode decreased from 650 mV to 550 mV vs RHE, whereas the E_{oc} of the p-InP/Nb_2O_5/Pt electrodes remained at ~350 mV vs RHE (Figure 2a). Mott-Schottky analysis indicated that the flat-band potential in contact with 1.0 M H_2SO_4(aq) was 0.96 V, 0.89 V, and 0.82 V vs RHE, respectively, for p-InP/Pt, p-InP/TiO_2/Pt, and p-InP/Nb_2O_5/Pt electrodes (Figure S1b). Compared to platinized Ni electrodes, Ni/TiO_2/Pt and Ni/Nb_2O_5/Pt electrodes exhibited overpotentials of ~100 mV and ~150 mV, respectively, for reduction of protons in 1.0 M H_2SO_4(aq) (Figure S5b), although the Ni/TiO_2/Pt electrodes appeared to be more resistive than the Ni/Nb_2O_5/Pt electrodes at comparable thicknesses of these two oxide films. This behavior is consistent with expectations for $E_{cb}(TiO_2)$ ~0.1-0.2 V vs RHE, whereas $E_{cb}(Nb_2O_5)$ is ~ -0.3 V vs RHE.

After 24 h at 0 V vs RHE under continuous 100 mW cm^{-2} of simulated solar illumination, p-InP and p-InP/Pt electrodes showed XPS emissions ascribable to In^0 and InO_x (Figure S11 and S12). No In XPS emissions were detectable on either the p-InP/Nb_2O_5/Pt or p-InP/Nb_2O_5 electrodes following 24 h of continuous illumination at 0 V vs RHE (Figure S11 and S12). p-InP/Nb_2O_5/Pt and p-InP/Pt electrodes both showed emissions ascribable to In^0/InO_x after 24 h in the dark at E_{oc} (Figure S13).

Scanning electron micrographs (SEM) showed substantial corrosion and roughening of the surface of etched p-InP held under illumination at 0 V vs RHE in 1.0 M H_2SO_4(aq), whereas under the same conditions the corrosion of p-InP/Nb_2O_5 electrodes was confined to pinholes where the Nb_2O_5 layer did not fully cover the p-InP substrate (Figure S14).

The chemical and anodic dissolution corrosion behavior was quantified by inductively coupled mass spectrometry (ICP-MS) data for p-InP, p-InP/Pt, p-InP/Nb_2O_5, and p-InP/Nb_2O_5/Pt electrodes held under 100 mW cm^{-2} of simulated solar illumination for 24 h at 0 V vs RHE as well as for electrodes held at open-circuit in the dark (Figure 3). Etched p-InP electrodes exhibited an order of magnitude greater dissolved In^{3+} in the solution than did the kinetically stabilized p-InP/Pt electrodes (Figure 3a). For the electrodes held at open-circuit in the dark, the E_{oc} for p-InP/Pt electrodes varied from -0.2 V vs RHE to 0.3 V vs RHE, whereas E_{oc} for p-InP/Nb_2O_5/Pt electrodes varied from -0.1 V vs RHE to 0.05 V vs RHE. In the dark at open circuit, the dissolution rate of p-InP/Pt electrodes was 2.3 nm h^{-1}, whereas p-InP/Nb_2O_5/Pt electrodes exhibited a dissolution rate of <0.05 nm h^{-1} (Figure 3b). Table S4 lists the current density, photovoltage, and dissolution rates obtained from the experiments in this work. Specifically, the ALD-coated Nb_2O_5 films substantially reduce the rates of the primary failure mode of p-InP photocathodes. The Nb_2O_5 films thus block interfacial hole transfer and suppress the primary failure mode of p-InP electrodes in the dark in addition to facilitating kinetic stabilization of the photoelectrode for the HER under illumination.[12] The remaining dissolution is ascribable to pinholes that are known to occur on oxide films deposited in air using ALD to form protection layers for photoanodes.[28] In contrast to phenomenological measurements of photocurrent stability, measurements of the rate of the primary dissolution failure mode in both the light and dark presented herein allow quantitative

calculation of the durability of these protected photocathodes for any combination of selected operational conditions and substrate thicknesses.

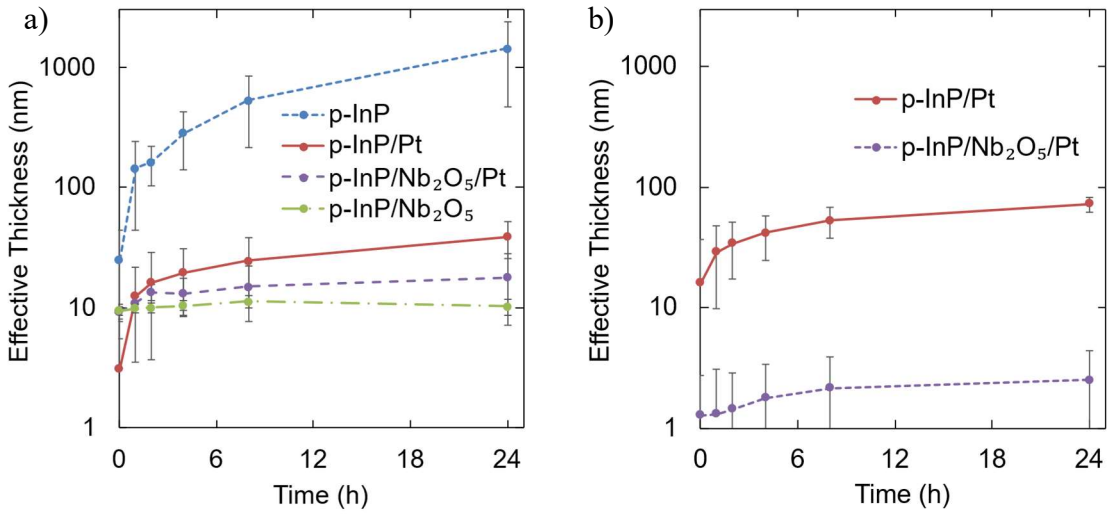

Figure 3. ICP-MS data of the (a) effective dissolution thickness of p-InP over time during 24 h at 0 V vs RHE, and (b) effective dissolution thickness of p-InP over time during 24 h at open circuit in the dark.

Discussion

The differences between the photovoltages of the etched, TiO_2-coated, and Nb_2O_5-coated p-InP photocathodes can be primarily attributed to differences in E_{fb} in conjunction with differences in the energetic barriers between the metal oxide protection layer and the solution (Figure S4 and S6). $E_{cb}(Nb_2O_5) < E(V^{3+/2+})$, so reduction of V^{3+} to V^{2+} by electrons photoinjected into the Nb_2O_5 protection layer is thermodynamically favorable. The *J-E* behavior of Ni/Nb_2O_5 electrodes shows residual kinetic barriers for V^{3+} reduction that result in ~250 mV overpotential to produce cathodic current densities of 1-10 mA cm^{-2} (Figure S5a). In contrast, $E_{cb}(TiO_2) > E(V^{3+/2+})$, so reduction of V^{3+} by photoinjected electrons in the TiO_2 protection layer has both thermodynamic and kinetic

barriers (Figure S4 and S6). Consistently, the *J-E* behavior of Ni/TiO_2 electrodes shows a ~400 mV overpotential to produce cathodic current densities of 1-10 mA cm^{-2} for reduction of V^{3+} in 5.0 M HCl(aq) (Figure S5a). $E_{cb}(TiO_2)$ is close to $E(H^+/H_2)$ and $E_{cb}(Nb_2O_5) < E(H^+/H_2)$, so Ni/$TiO_2$/Pt and Ni/$Nb_2O_5$/Pt interfaces exhibit lower overpotentials for H^+ reduction than for reduction of V^{3+} (Figure S4, S5b, and 6c). Metals with a low work-function, such as Ni, yield low interfacial barriers for hole conduction at TiO_2/1.0 M KOH(aq) interfaces relative to metals with a high work function, such as Ir, that form rectifying contacts to TiO_2 deposited by ALD and thus yield low photovoltages for O_2(g) production in 1.0 M KOH(aq).[10] Hence, optimization of the interfacial charge-transfer kinetics between the protection layer and 1.0 M H_2SO_4(aq) would be expected to minimize the ~100 mV and ~150 mV interfacial overpotentials of the p-InP/TiO_2/Pt and p-InP/Nb_2O_5/Pt photocathodes, respectively, for the HER in 1.0 H_2SO_4(aq) (Figure S5b).[54]

The remaining difference in photovoltage between the various protected p-InP photocathodes arises predominantly from the electrical characteristics of the interface between the p-InP and the oxide protection layer. In contact with 1.0 M H_2SO_4(aq), the open-circuit voltage of p-InP/Nb_2O_5/Pt photocathodes is lower than that of p-InP/Pt photocathodes. However, the photovoltage of p-InP electrodes is beneficially affected by formation of a submonolayer of interfacial InO.[30,55] For example, a photovoltage of ~0.65 V is obtained when titanium (IV) isopropoxide (TTIP) is used as the ALD precursor to form TiO_2 protection layers on p-InP photocathodes.[56] Hence, interfacial engineering of the intervening oxide through the insertion of ultrathin layers or interfacial dipoles and of the InP band-edge positions could improve the photovoltage of the p-InP/Nb_2O_5/Pt photoelectrodes while retaining the beneficial stability characteristics of the Nb_2O_5 protection layer. Improvement of the metal oxide/catalyst contact through careful selection of catalyst deposition method and composition may also minimize the

overpotentials at the oxide/catalyst/liquid interface. Due to the large pH stability window of Nb_2O_5, Nb_2O_5 may be also suitable as a protection layer for a variety of solar fuels reduction reactions such as N_2 reduction or CO_2 reduction. Moreover, p-GaInP shares primary failure modes with p-InP, but p-GaInP is more resistant to metal plating than p-InP due to the more negative plating potential of Ga relative to In.[7,57] Hence, extension of Nb_2O_5 protection layers to p-GaInP, which has a near-optimal band gap of $\mathbf{E}_g$ = 1.7 eV for use in a tandem photoelectrode structure for fuel formation,[6,16,17,20] should reasonably be expected. Stabilization of p-GaInP would therefore provide a last missing component of a first-generation prototype tandem full photoelectrochemical cell that efficiently splits water for extended periods of time into separate streams of H_2 and O_2.[6,17,58,59]

Conclusions

In summary, ALD-deposited barrier layers suitable for the protection of photocathodes need to conduct photogenerated electrons, block interfacial transfer of holes, and be stable in acidic or alkaline solutions at potentials near RHE. The band alignment between Nb_2O_5 and p-InP facilitates conduction of photogenerated minority carriers through the protection layer, to effect fuel-forming reductive half-reactions. The Nb_2O_5 blocks interfacial hole transfer and consequently inhibits anodic dissolution of p-InP photocathodes, resulting in a lower rate of InP dissolution in the dark at open circuit than kinetically stabilized p-InP photocathodes, which are cathodically protected only under illumination. Furthermore, Nb_2O_5 is stable over the range of negative potentials and pH values required for efficient, safe water splitting. In contrast to TiO_2, Nb_2O_5 does not rapidly dissolve at RHE in acidic aqueous electrolytes. Moreover, the shift in E_{cb} of Nb_2O_5 advantageously minimizes the electrochromism, blue-coloration and trap-state filling at potentials near RHE where the reductive half-reactions for fuel formation proceed, and additionally minimizes the energetic

barrier for photogenerated minority-carrier electrons to reduce water to H_2 relative to the energies of the trap-state levels or the conduction-band edge energy of the oxide in the protection layer. The data demonstrate that the interfacial charge flows predominantly through the Nb_2O_5 films and moreover allow quantitative evaluation of the effects of residual pinholes in the film on suppressing the primary failure mode, anodic and/or chemical dissolution, of p-InP photocathodes being used for hydrogen evolution in acid. The protocols described in this work should also be useful in identification of other barrier layer materials for photocathode protection.

ASSOCIATED CONTENT

Supporting Information

Mott-Schottky data, *J-E* plots, XPS data, UV-Vis data, and SEM data.

AUTHOR INFORMATION

Authors

Alexandre Z. Ye – Division of Chemistry and Chemical Engineering, California Institute of Technology, Pasadena, CA 91125, United States;

Dominic Covelli – Division of Chemistry and Chemical Engineering, California Institute of Technology, Pasadena, CA 91125, United States;

Ariel A. Struzyk – Division of Chemistry and Chemical Engineering, California Institute of Technology, Pasadena, CA 91125, United States;

Paul J. L. Bean – Division of Chemistry and Chemical Engineering, California Institute of Technology, Pasadena, CA 91125, United States;

Xinyi Elaine Shen – Division of Chemistry and Chemical Engineering, California Institute of Technology, Pasadena, CA 91125, United States;

Nathan S. Lewis – Division of Chemistry and Chemical Engineering, California Institute of Technology, Pasadena, CA 91125, United States; Beckman Institute, California Institute of Technology, Pasadena, CA 91125, United States; Email: nslewis@caltech.edu

Notes

The authors declare no competing financial interest.

ACKNOWLEDGEMENTS

This work was supported through the Office of Science of the U.S. Department of Energy under Award Number DE-FG02-03-ER15483 from the Basic Energy Sciences Office of the DOE. Research was in part carried out at the Molecular Materials Research Center of the Beckman Institute of the California Institute of Technology.

REFERENCES

(1) Walter, M. G.; Warren, E. L.; McKone, J. R.; Boettcher, S. W.; Mi, Q.; Santori, E. A.; Lewis, N. S. Solar Water Splitting Cells. *Chem. Rev.* **2010**, *110* (11), 6446–6473.

(2) McKone, J. R.; Lewis, N. S.; Gray, H. B. Will Solar-Driven Water-Splitting Devices See the Light of Day? *Chem. Mater.* **2014**, *26* (1), 407–414.

(3) *Semiconductor Electrodes*; Finklea, H. O., Ed.; Studies in physical and theoretical chemistry; Elsevier: Amsterdam ; New York, 1988.

(4) Bae, D.; Seger, B.; Vesborg, P. C. K.; Hansen, O.; Chorkendorff, I. Strategies for Stable Water Splitting via Protected Photoelectrodes. *Chem. Soc. Rev.* **2017**, *46* (7), 1933–1954.

(5) Hu, S.; Shaner, M. R.; Beardslee, J. A.; Lichterman, M.; Brunschwig, B. S.; Lewis, N. S. Amorphous TiO_2 Coatings Stabilize Si, GaAs, and GaP Photoanodes for Efficient Water Oxidation. *Science* **2014**, *344* (6187), 1005–1009.

(6) Hu, S.; Lewis, N. S.; Ager, J. W.; Yang, J.; McKone, J. R.; Strandwitz, N. C. Thin-Film Materials for the Protection of Semiconducting Photoelectrodes in Solar-Fuel Generators. *J. Phys. Chem. C* **2015**, *119* (43), 24201–24228.

(7) Pourbaix, M. *Atlas of Electrochemical Equilibria in Aqueous Solutions*; National Assoc. of Corrosion Engineers: Houston, TX, 1974.

(8) Shen, X.; Yao, M.; Sun, K.; Zhao, T.; He, Y.; Chi, C.-Y.; Zhou, C.; Dapkus, P. D.; Lewis, N. S.; Hu, S. Defect-Tolerant TiO_2-Coated and Discretized Photoanodes for >600 h of Stable Photoelectrochemical Water Oxidation. *ACS Energy Lett.* **2021**, *6* (1), 193–200.

(9) Hu, S.; Richter, M. H.; Lichterman, M. F.; Beardslee, J.; Mayer, T.; Brunschwig, B. S.; Lewis, N. S. Electrical, Photoelectrochemical, and Photoelectron Spectroscopic Investigation of the Interfacial Transport and Energetics of Amorphous TiO_2/Si Heterojunctions. *J. Phys. Chem. C* **2016**, *120* (6), 3117–3129.

(10) Nunez, P.; Richter, M. H.; Piercy, B. D.; Roske, C. W.; Cabán-Acevedo, M.; Losego, M. D.; Konezny, S. J.; Fermin, D. J.; Hu, S.; Brunschwig, B. S.; Lewis, N. S. Characterization of Electronic Transport through Amorphous TiO_2 Produced by Atomic Layer Deposition. *J. Phys. Chem. C* **2019**, *123* (33), 20116–20129.

(11) Shaner, M. R.; Hu, S.; Sun, K.; Lewis, N. S. Stabilization of Si Microwire Arrays for Solar-Driven H_2O Oxidation to O_2(g) in 1.0 M KOH(aq) Using Conformal Coatings of Amorphous TiO_2. *Energy Environ. Sci.* **2015**, *8* (1), 203–207.

(12) Yu, W.; Richter, M. H.; Buabthong, P.; Moreno-Hernandez, I. A.; Read, C. G.; Simonoff, E.; Brunschwig, B. S.; Lewis, N. S. Investigations of the Stability of Etched or Platinized p-InP(100) Photocathodes for Solar-Driven Hydrogen Evolution in Acidic or Alkaline Aqueous Electrolytes. *Energy Environ. Sci.* **2021**, *14* (11), 6007–6020.

(13) Yu, W.; Young, J. L.; Deutsch, T. G.; Lewis, N. S. Understanding the Stability of Etched or Platinized p-GaInP Photocathodes for Solar-Driven H_2 Evolution. *ACS Appl. Mater. Interfaces* **2021**, *13* (48), 57350–57361.

(14) Yu, W.; Richter, M. H.; Simonoff, E.; Brunschwig, B. S.; Lewis, N. S. Investigations of the Stability of GaAs for Photoelectrochemical H_2 Evolution in Acidic or Alkaline Aqueous Electrolytes. *J. Mater. Chem. A* **2021**, *9* (40), 22958–22972.

(15) Gerischer, H. On the Stability of Semiconductor Electrodes against Photodecomposition. *J. Electroanal. Chem. Interf. Electrochem.* **1977**, *82* (1–2), 133–143.

(16) Hu, S.; Xiang, C.; Haussener, S.; Berger, A. D.; Lewis, N. S. An Analysis of the Optimal Band Gaps of Light Absorbers in Integrated Tandem Photoelectrochemical Water-Splitting Systems. *Energy Environ. Sci.* **2013**, *6* (10), 2984.

(17) Tournet, J.; Lee, Y.; Karuturi, S. K.; Tan, H. H.; Jagadish, C. III–V Semiconductor Materials for Solar Hydrogen Production: Status and Prospects. *ACS Energy Lett.* **2020**, *5* (2), 611–622.

(18) Schulte, K. H.; Lewerenz, H. J. Combined Photoelectrochemical Conditioning and Photoelectron Spectroscopy Analysis of InP Photocathodes: I. The Modification Procedure. *Electrochim. Acta* **2002**, *47* (16), 2633–2638.

(19) Lewerenz, H. J.; Schulte, K. H. Combined Photoelectrochemical Conditioning and Surface Analysis of InP Photocathodes: II. Photoelectron Spectroscopy. *Electrochim. Acta* **2002**, *47* (16), 2639–2651.

(20) Britto, R. J.; Benck, J. D.; Young, J. L.; Hahn, C.; Deutsch, T. G.; Jaramillo, T. F. Molybdenum Disulfide as a Protection Layer and Catalyst for Gallium Indium Phosphide Solar Water Splitting Photocathodes. *J. Phys. Chem. Lett.* **2016**, *7* (11), 2044–2049.

(21) Heller, A.; Vadimsky, R. G. Efficient Solar to Chemical Conversion: 12% Efficient Photoassisted Electrolysis in the [p-type InP(Ru)]/HCl-KCl/Pt(Rh) Cell. *Phys. Rev. Lett.* **1981**, *46* (17), 1153–1156.

(22) Gerischer, H. Photodecomposition of Semiconductors Thermodynamics, Kinetics and Application to Solar Cells. *Faraday Discuss. Chem. Soc.* **1980**, *70*, 137.

(23) Lee, M. H.; Takei, K.; Zhang, J.; Kapadia, R.; Zheng, M.; Chen, Y.-Z.; Nah, J.; Matthews, T. S.; Chueh, Y.-L.; Ager, J. W.; Javey, A. p-type InP Nanopillar Photocathodes for Efficient Solar-Driven Hydrogen Production. *Angew. Chem. Int. Ed.* **2012**, *51* (43), 10760–10764.

(24) Malizia, M.; Seger, B.; Chorkendorff, I.; Vesborg, P. C. K. Formation of a p–n Heterojunction on GaP Photocathodes for H_2 Production Providing an Open-Circuit Voltage of 710 mV. *J. Mater. Chem. A* **2014**, *2* (19), 6847–6853.

(25) Arunachalam, M.; Subhash Kanase, R.; Ganapati Badiger, J.; Abdelfattah Sayed, S.; Ahn, K.-S.; Ha, J.-S.; Ryu, S.-W.; Hyung Kang, S. Durable Bias-Free Solar Water-Splitting Cell Composed of n^+p-Si/Nb_2O_5/NiPt Photocathode and W:$BiVO_4$/$NiCo(O\text{-}OH)_2$ Photoanode. *Chem. Eng. J.* **2023**, *474*, 145262.

(26) Warren, E. L.; McKone, J. R.; Atwater, H. A.; Gray, H. B.; Lewis, N. S. Hydrogen-Evolution Characteristics of Ni–Mo-Coated, Radial Junction, n^+p-Silicon Microwire Array Photocathodes. *Energy Environ. Sci.* **2012**, *5* (11), 9653.

(27) Roske, C. W.; Popczun, E. J.; Seger, B.; Read, C. G.; Pedersen, T.; Hansen, O.; Vesborg, P. C. K.; Brunschwig, B. S.; Schaak, R. E.; Chorkendorff, I.; Gray, H. B.; Lewis, N. S. Comparison of the Performance of CoP-Coated and Pt-Coated Radial Junction n^+p-Silicon Microwire-Array Photocathodes for the Sunlight-Driven Reduction of Water to H_2(g). *J. Phys. Chem. Lett.* **2015**, *6* (9), 1679–1683.

(28) Buabthong, P.; Ifkovits, Z. P.; Kempler, P. A.; Chen, Y.; Nunez, P. D.; Brunschwig, B. S.; Papadantonakis, K. M.; Lewis, N. S. Failure Modes of Protection Layers Produced by Atomic Layer Deposition of Amorphous TiO_2 on GaAs Anodes. *Energy Environ. Sci.* **2020**, *13* (11), 4269–4279.

(29) Justin Gorham. NIST X-Ray Photoelectron Spectroscopy Database - SRD 20, 2012.

(30) Heller, A.; Miller, B.; Thiel, F. A. 11.5% Solar Conversion Efficiency in the Photocathodically Protected *p*-InP/V^{3+}-V^{2+}-HCl/C Semiconductor Liquid Junction Cell. *Appl. Phys. Lett.* **1981**, *38* (4), 282–284.

(31) Michaelis, L.; Hill, E. S. The Viologen Indicators. *J. Gen. Physiol.* **1933**, *16* (6), 859–873.

(32) Arman, M. Ö.; Geboes, B.; Van Hecke, K.; Binnemans, K.; Cardinaels, T. Kinetics of Electrochemical Eu^{3+} to Eu^{2+} Reduction in Aqueous Media. *Electrochim. Acta* **2024**, *484*, 144055.

(33) Smith, W. A.; Sharp, I. D.; Strandwitz, N. C.; Bisquert, J. Interfacial Band-Edge Energetics for Solar Fuels Production. *Energy Environ. Sci.* **2015**, *8* (10), 2851–2862.

(34) Robertson, J.; Chen, C. W. Schottky Barrier Heights of Tantalum Oxide, Barium Strontium Titanate, Lead Titanate, and Strontium Bismuth Tantalate. *Appl. Phys. Lett.* **1999**, *74* (8), 1168–1170.

(35) Wilk, G. D.; Wallace, R. M.; Anthony, J. M. High-κ Gate Dielectrics: Current Status and Materials Properties Considerations. *J. Appl. Phys.* **2001**, *89* (10), 5243–5275.

(36) Rothenberger, G.; Fitzmaurice, D.; Graetzel, M. Spectroscopy of Conduction Band Electrons in Transparent Metal Oxide Semiconductor Films: Optical Determination of the Flatband Potential of Colloidal Titanium Dioxide Films. *J. Phys. Chem.* **1992**, *96* (14), 5983–5986.

(37) Lyon, L. A.; Hupp, J. T. Energetics of the Nanocrystalline Titanium Dioxide/Aqueous Solution Interface: Approximate Conduction Band Edge Variations between $H_0 = -10$ and $H_- = +26$. *J. Phys. Chem. B* **1999**, *103* (22), 4623–4628.

(38) Basuvalingam, S. B.; Macco, B.; Knoops, H. C. M.; Melskens, J.; (Erwin) Kessels, W. M. M.; Bol, A. A. Comparison of Thermal and Plasma-Enhanced Atomic Layer Deposition of Niobium Oxide Thin Films. *J. Vac. Sci. Technol. A* **2018**, *36* (4), 041503.

(39) Blanquart, T.; Niinistö, J.; Heikkilä, M.; Sajavaara, T.; Kukli, K.; Puukilainen, E.; Xu, C.; Hunks, W.; Ritala, M.; Leskelä, M. Evaluation and Comparison of Novel Precursors for Atomic Layer Deposition of Nb_2O_5 Thin Films. *Chem. Mater.* **2012**, *24* (6), 975–980.

(40) Portier, J.; Hilal, H.; Saadeddin, I.; Hwang, S.; Subramanian, M.; Campet, G. Thermodynamic Correlations and Band Gap Calculations in Metal Oxides. *Prog. Solid State Chem.* **2004**, *32* (3–4), 207–217.

(41) Reyes-Coronado, D.; Rodríguez-Gattorno, G.; Espinosa-Pesqueira, M. E.; Cab, C.; De Coss, R.; Oskam, G. Phase-Pure TiO_2 Nanoparticles: Anatase, Brookite and Rutile. *Nanotechnology* **2008**, *19* (14), 145605.

(42) Mavroides, J. G. Electrode Materials for the Photoelectrolysis of Water. *Mater. Res. Bull.* **1978**, *13* (12), 1379–1388.

(43) Kung, H. H.; Jarrett, H. S.; Sleight, A. W.; Ferretti, A. Semiconducting Oxide Anodes in Photoassisted Electrolysis of Water. *J. Appl. Phys.* **1977**, *48* (6), 2463–2469.

(44) Chen, S.; Wang, L.-W. Thermodynamic Oxidation and Reduction Potentials of Photocatalytic Semiconductors in Aqueous Solution. *Chem. Mater.* **2012**, *24* (18), 3659–3666.

(45) Hoffeditz, W. L.; Pellin, M. J.; Farha, O. K.; Hupp, J. T. Determining the Conduction Band-Edge Potential of Solar-Cell-Relevant Nb_2O_5 Fabricated by Atomic Layer Deposition. *Langmuir* **2017**, *33* (37), 9298–9306.

(46) Buabthong, P.; Evans, J. M.; Rinaldi, K. Z.; Kennedy, K. M.; Fu, H. J.; Ifkovits, Z. P.; Kuo, T.-J.; Brunschwig, B. S.; Lewis, N. S. GaAs Microisland Anodes Protected by Amorphous TiO_2 Films Mitigate Corrosion Spreading During Water Oxidation in Alkaline Electrolytes. *ACS Energy Lett.* **2021**, *6* (10), 3709–3714.

(47) Nowak, I.; Ziolek, M. Niobium Compounds: Preparation, Characterization, and Application in Heterogeneous Catalysis. *Chem. Rev.* **1999**, *99* (12), 3603–3624.

(48) Jain, A.; Ong, S. P.; Hautier, G.; Chen, W.; Richards, W. D.; Dacek, S.; Cholia, S.; Gunter, D.; Skinner, D.; Ceder, G.; Persson, K. A. Commentary: The Materials Project: A Materials Genome Approach to Accelerating Materials Innovation. *APL Materials* **2013**, *1* (1), 011002.

(49) Patel, A. M.; Nørskov, J. K.; Persson, K. A.; Montoya, J. H. Efficient Pourbaix Diagrams of Many-Element Compounds. *Phys. Chem. Chem. Phys.* **2019**, *21* (45), 25323–25327.

(50) Boschloo, G.; Fitzmaurice, D. Spectroelectrochemical Investigation of Surface States in Nanostructured TiO_2 Electrodes. *J. Phys. Chem. B* **1999**, *103* (12), 2228–2231.

(51) Reichman, B.; Bard, A. J. Electrochromism at Niobium Pentoxide Electrodes in Aqueous and Acetonitrile Solutions. *J. Electrochem. Soc.* **1980**, *127* (1), 241–242.

(52) ANSI C78.1431-1997 (S2022), 2022.

(53) Tawfik, M.; Tonnellier, X.; Sansom, C. Light Source Selection for a Solar Simulator for Thermal Applications: A Review. *Renew. Sustain. Energy Rev.* **2018**, *90*, 802–813.

(54) Kaufman, A. J.; Krivina, R. A.; Shen, M.; Boettcher, S. W. Controlling Catalyst–Semiconductor Contacts: Interfacial Charge Separation in p-InP Photocathodes. *ACS Energy Lett.* **2022**, *7* (1), 541–549.

(55) Suzuki, T.; Ogawa, M. *In Situ* Measurements of Photoluminescence Intensities from Cleaved (110) Surfaces of *n*-Type InP in a Vacuum and Gas Ambients. *Appl. Phys. Lett.* **1979**, *34* (7), 447–449.

(56) Lin, Y.; Kapadia, R.; Yang, J.; Zheng, M.; Chen, K.; Hettick, M.; Yin, X.; Battaglia, C.; Sharp, I. D.; Ager, J. W.; Javey, A. Role of TiO_2 Surface Passivation on Improving the Performance of p-InP Photocathodes. *J. Phys. Chem. C* **2015**, *119* (5), 2308–2313.

(57) Bard, A. J.; Parsons, R.; Jordan, J. *Standard Potentials in Aqueous Solution*, 1st ed.; Routledge, 2017.

(58) Lewis, N. S.; Nocera, D. G. Powering the Planet: Chemical Challenges in Solar Energy Utilization. *Proc. Natl. Acad. Sci. U.S.A.* **2006**, *103* (43), 15729–15735.

(59) Lewis, N. S. Developing a Scalable Artificial Photosynthesis Technology through Nanomaterials by Design. *Nature Nanotech.* **2016**, *11* (12), 1010–1019.